Generating a missing half of multifractal fields with a blunt extension of discrete cascades

Auguste Gires, Ioulia Tchiguirinskaia, Daniel Schertzer

Generating a missing half of multifractal fields with a blunt extension of discrete cascades

Auguste Gires, Ioulia Tchiguirinskaia, Daniel Schertzer

Hydrologie Météorologie et Complexité, Ecole des Ponts ParisTech, Champs-sur-Marne, France

* Corresponding author: auguste.gires@enpc.fr

Generating a missing half of multifractal fields with a blunt extension of discrete cascades

Despite strong limitations, discrete random multiplicative cascades are often used to address scale issues which are ubiquitous in geosciences. A blunt extension based on the parsimonious framework of Universal Multifractals has recently been suggested. It preserves its simplicity and intuitiveness while overcoming its non-stationarity features. It relies on smoothing through a geometrical moving average the increments at each cascade step. Here a space-time extension is suggested. Theoretically expected multifractal behaviour is retrieved on numerical simulations for typical rainfall parameters. A new algorithm to generate the missing half of multifractal fields in 1D, 2D or 3D is developed and tested on rainfall fields and numerical simulations. It basically consists in stochastically generating half of the increments and deterministically iteratively reconstructing the others to retrieve the available data and ensure a smooth transition with the unknown portion while preserving the multifractal behaviour. Potential applications to nowcasting of hydro-meteorological extremes are discussed.

Keywords: word; another word; lower case except names

Introduction

The use of multiplicative cascades to model turbulence emerged from the need to better understand the underlying processes and notably the consequences of Navier-Stokes equations' scale invariance (Kolmogorov 1941). Given that these features are assumed to be transferred to the (unknown) equations governing other atmospheric fields such as rainfall for example (Schertzer and Lovejoy 1987, Hubert et al. 2001), scale issues are ubiquitous in atmospheric sciences and more generally in geosciences. Universal Multifractals (UM, see Schertzer and Tchiguirinskaia 2020 for recent review) are a theoretical framework relying on this concept which enables to characterize and simulate geophysical fields exhibiting extreme variability over wide range of space-time scales, with the help of only three parameters with physical meaning. In such process,

an average intensity, homogeneously distributed over a large scale structure, is iteratively distributed in space and time to smaller scale structures.

Because they are simple and intuitive, discrete multiplicative cascades have been extensively used in geosciences Gupta and Waymire 1993, Over and Gupta 1996, Olsson 1998, Menabde and Sivapalan 2000, Gaume et al. 2007, Licznar et al. 2011, Rupp et al. 2012, Gires et al. 2013, Müller and Haberlandt 2016). At each step (i) of such process, a structure is divided into λ_1^d sub-structures (d is dimension of the embedding space). The intensity affected to a sub-structure is equal to the intensity of the parent structure multiplied by a random 'multiplicative increment' denoted b_i. Such cascade step is then iteratively repeated. Hence, after n steps, i.e. at resolution $\lambda = \lambda_1^n = \lambda_n$ (the resolution λ is defined as the ratio between the outer scale L and the observation scale l; $\lambda = L/l$, a value of the generated field ε_n is equal to the product of all the corresponding multiplicative increments:

$$\varepsilon_n = \varepsilon_0 \prod_{i=1}^{n} (b_i) \qquad (1)$$

The complex space-time variability naturally arises from the iteration of a simple cascade step. The process is said to be scale invariant because the way structures are divided into substructures and the probability distribution of the random multiplicative increments are the same at all scales (i.e. cascade steps). It should be mentioned that this scale discretisation is not physical which is why Schertzer and Lovejoy (1987) suggested to overcome such limitation by introducing continuous in scale cascades. A kind of intermediate solution enabling to address the lack of stationarity of discrete cascades while preserving its simple structure was introduced recently by Gires et al. (2020). It basically consists in introducing at each cascade step

the final resolution and performing a geometric interpolation of the increments over moving windows whose size is tuned at each scale to preserve scale invariance. It is called blunt extension of discrete cascades and will be further developed and used in this paper.

On the other hand, the issue of missing data has also become ubiquitous and crucial, notably because of the extensive development of data driven approaches and the need to validate model at higher and higher resolution. The interested reader is referred to Ben Aissia et al. (2017) for a recent review in the field of hydrology, keeping in mind that the topic goes beyond geosciences (Garciarena and Santana 2017). A solution explored by various authors to infill missing data is to rely on the underlying scaling features of the studied field (Salvadori et al. 2000, Tchiguirinskaia et al. 2004 , Gires et al 2021). Gires et al. (2021) specifically used discrete cascades to achieve this for binary fields. More precisely they used a β-model (Frisch et al. 1978), i.e. the simplest possible discrete cascade process where the increments have only two possible values (zero or one). Reconstructing a field from an underlying cascade process requires to assess all the increment at the various cascade steps. Hence the overall idea suggested consisted in deterministically finding the increments needed so that the simulated fields had the expected value where data is available and stochastically simulating the others while ensuring the expected fractal behaviour is retrieved. The process was then successfully implemented on rainfall occurrence patterns and imperviousness maps.

In this paper, we suggest a new algorithm to generate the missing half of a multifractal field, i.e. the next time steps of a time series in 1D, the adjacent map in 2D or the maps for the next time steps in a space-time framework. If the process is applied to the specific context of real time applications, i.e. guessing what will happen in the coming minutes, it is called nowcasting in the field of geoscience. For rainfall

applications, continuous cascades have been used for this (Macor 2007), and also with other approaches involving some scale invariant features (Seed et al. 2003, Bowler et al. 2006). In this paper, it is assumed that the underlying field exhibits UM features, i.e. that it can be generated through a blunt discrete UM cascade process. One should note that the issue of guessing the missing half of a field is actually a sort of extreme case of infilling missing data where half of the field is missing. Hence, as in Gires et al. (2021), the whole purpose is to assess a set of increments enabling to generate a field that has the expected value on the available half and exhibits the expected same multifractal behaviour on the other half. In a similar way, some increments will be stochastically generated while the others will be deterministically reconstructed.

In section 2, the framework of blunt discrete UM cascades will be extended to space-time process, which notably requires to properly address the tricky issue of increments renormalization. In section 3, a new algorithm to generate the missing half of a multifractal field is suggested. The algorithm is then implemented and validated in section 4, first in 1D with rainfall disdrometer time series, then in 2D with rainfall weather radar maps and finally in a space-time context with numerical simulations.

Space-time blunt extension of UM discrete cascades

Reminder on UM discrete cascades

Only the required elements on the framework of Universal Multifractals (UM), which were already presented similarly in Gires et al. (2020) are reminded here and the interested reader is referred to a recent review by Schertzer and Tchiguirinskaia (2020) for more details.

Let us consider a field B_λ at a resolution λ. For multifractal fields, the moment of order q of the field is power law related to the resolution:

$$\left\langle B_\lambda^q \right\rangle \approx \lambda^{K(q)} \qquad (2)$$

where $K(q)$ is the scaling moment function that fully characterizes the variability across scales of the field. In the specific framework of Universal Multifractals (UM) (Schertzer and Lovejoy, 1987; 1997), towards which multiplicative cascades processes converge, $K(q)$ for conservative fields is defined with the help of only two parameters with physical interpretation:

- C_1, the mean intermittency co-dimension, which measures the clustering of the (average) intensity at smaller and smaller scales. $C_1 = 0$ for a homogeneous field;
- α, the multifractality index ($0 \le \alpha \le 2$), which measures the clustering variability with regards to the intensity level.

For UM, we have:

$$K(q) = \frac{C_1}{\alpha - 1}(q^\alpha - q) \qquad (3)$$

A multifractal analysis consists in checking that these features are indeed observed. The quality of the scaling can be assessed with the help of Trace Moment (TM) analysis which basically consists in plotting in log-log Eq. 1. Straight lines should be retrieved and the slope gives $K(q)$. The field at various resolution is obtained by up-scaling to lower resolution the field measured at its maximum resolution. It should be stressed that such process does not enable to retrieve the exact values of the increments used for generating a field. See Schertzer and Lovejoy (1987) for a complete discussion of the difference between what is denoted in the literature bare (obtained during the generation) and dressed (obtained after up-scaling from the maximum resolution) fields.

The Double Trace Moment (DTM) technique is tailored for UM fields and enables robust estimation of UM parameters (Lavallée et al., 1993). Hence it will be used in this paper. More precisely, it relies on the fact the field $B_\lambda^{(\eta)}$, obtained by up-scaling the field raised to the power η at maximum resolution , scales as :

¿ (4)

and in the UM framework, we have:

$$K(q,\eta)=\eta^{\alpha}K(q) \qquad (5)$$

In a DTM analysis, $K(q,\eta)$ is first obtained by plotting Eq. 4 in log-log. The slope of the retrieved line gives$K(q,\eta)$. The quality of the linear regression gives an indication on the quality of the scaling behaviour of the studied field. Then $K(q,\eta)$ is plotted against η in log-log and the slope and intercept of the linear portion give access to α and C_1 respectively.

It is possible to generate UM fields with the help of discrete multiplicative cascades as described in the introduction. We start by a large scale structure with a given intensity B_0 and take the random increment b as:

$$b=\frac{\exp\left[\left(\frac{C_1\ln\lambda_1}{|\alpha-1|}\right)^{1/\alpha}L(\alpha)\right]}{\lambda_1^{\frac{C_1}{\alpha-1}}} \qquad (6)$$

where $L(\alpha)$ is an extremal Lévy-stable random variable of index α. It is generated with the help of the procedure given by Chambers et al. (1976), and has the following property:

$$\langle\exp\left[qL(\alpha)\right]\rangle=\exp\left[q^{\alpha}\right] \qquad (7)$$

Combining Eqs. 7 and 8, we find:

$$\langle b^q \rangle = \frac{\left\langle \exp\left[q \left(\frac{C_1 \ln \lambda_1}{|\alpha - 1|} \right)^{1/\alpha} L(\alpha) \right] \right\rangle}{\lambda_1^{q \frac{C_1}{\alpha - 1}}} = \lambda_1^{\frac{C_1}{\alpha - 1}(q^\alpha - q)} \quad (8)$$

Finally, given that the increments b_i in Eq. 1 are independent and identically distributed, and keeping in mind that $\lambda_1^n = \lambda_n$ we can demonstrate that the field simulated is indeed a UM one :

$$\langle B_{n,i}^q \rangle = B_0^q \langle b^q \rangle^n = \lambda_n^{\frac{C_1}{\alpha - 1}(q^\alpha - q)} \quad (9)$$

For non-conservative fields, an additional parameter H called non-conservative parameter, is added and $H = 0$ for conservative fields. It can be either positive or negative. For a more practical interpretation, greater values H correspond to stronger correlations within the studied field. H is typically between 0 and 1 for geophysical fields. In this framework, a non-conservative fields ($B_\lambda^{'}$) is decomposed as follow:

$$B_\lambda^{'} \approx B_\lambda^{\square} \lambda^{-H} \quad (10)$$

Where $B_\lambda^{\square}$ is a conservative field and the portion corresponding to the variations of the average field has been separated. In such case the slope β of the spectra $E(k)$ (where *k* is the wave number)

$$E(k) \approx k^{-\beta} \quad (11)$$

is related to *H* as follows:

$$\beta = 1 + 2H - K(2) \quad (12)$$

Eq. 12 is used to estimate *H* after carrying out a spectral analysis (Eq. 11 in log-log) which is also an indicator of the quality of the scaling (Lavallée et al. 1993).

Blunt extension of UM discrete cascades

The blunt extension was introduced in details in Gires et al. (2020), and only the main and required elements are reminded here. Interested readers can refer to the cited paper for a more step by step introduction of this new process. The only difference with regards to Gires et al. (2020) is the renormalization of the increments. This point is specifically discussed in the next sub-section.

The overall idea of the blunt extension is straightforward: (i) introduce the final resolution at all the steps of the cascade process (ii) perform at each cascade step a geometric interpolation of the increments over adjacent increments (iii) renormalize the obtained increments. Detailed equations presented below may appear tricky but simply correspond to the implementation of the stated process.

The process is illustrated in Fig. 1 in 1D. Let us consider a standard discrete cascade process with *N* steps, hence corresponding to a total length of λ_1^N (usually $\lambda_1^{\square}=2$). Actually, in the blunt extension an average is made between over the two last cascade steps. Hence, $N+2$ steps need to be considered. The standard increments are denoted $b_{n,i}$, where n corresponds to the cascade step ($n \subset [1,\dots,N+2]$) and i to the position of the increment in the series for a given cascade step n ($i \subset [1,\dots,\lambda_1^n]$).

The first step of the process is to introduce the final resolution at each cascade step. Let us call l_{N+2} the length of a time step for the last cascade steps. Hence at cascade level *n*, the 'duration' corresponding to an increment is actually $l_n=\lambda_1^{N+2-n} l_{N+2}$. Indeed, the same total duration must be covered at each cascade step, meaning that we

have $l_n \lambda_1^n = \lambda_1^{N+2} l_{N+2}$. Introducing the final resolution will therefore simply consists in

repeating $\frac{l_n}{l_{N+2}} = \lambda_1^{N+2-n}$. times the same increment. This enables to have for each cascade steps a series of 2^{N+2} increments all corresponding to a duration of l_{N+2}. The standard increments can now be denoted $b_{n,j}$ where n corresponds to the cascade step ($n \subset [1,\ldots,N+2]$) and j to the position of the increment in the series for a given cascade step j ($j \subset [1,\ldots,\lambda_1^{N+2}]$). The final value of field for a given time step is then simply equal to the product of all the increments at each cascade steps for the same time step. It should be stressed that this manipulation does not affect at all the cascade process which for now remains identical to a standard one. It is not more than an update of the presentation.

The next step consists in performing at each cascade step a weighted geometric interpolation of the increments $b_{n,j}$ over moving windows of size s_n centred on it. This enables to smooth the sharp transitions between standard increments. A normalization is added to ensure that the wanted Universal Multifractal behaviour is retrieved. The new increment of this blunt extension is denoted $a_{n,j}$ and we have :

$$a_{n,j} = \frac{\prod_{k=1}^{s_n} b_{n,j-\frac{s_n-1}{2}+k}^{c_k}}{\lambda_1^{\frac{C_1}{\alpha-1}(S_{n,j}(\alpha,h)-1)}} \qquad (13)$$

where:

- c_k is the weight affected to each element of the moving window ($k \subset [1,\ldots,s_n]$).

  We have $\sum_{k=1}^{s_n} c_k = 1$. For practical implementation in the paper, we chose a

uniform distribution of the weight, i.e. $c_k = 1/s_n$. Nevertheless, the formalism is written in a generic way, meaning that more complex distributions can easily be tested.

- s_n is determined to remain in a scale invariant framework. More precisely, a new parameter h is introduced and corresponds to the number of 'true' adjacent increments (i.e. the $b_{n,i}$) over which the interpolation is computed. Practically, this yields $s_n = 1 + floor\left(h\,\lambda_1^{N+1-n}\right)$. The size of the moving window is basically always multiplied by the same factor doubles when going from one cascade step to the previous which is what is expected in a scale invariant framework. $h = 0$ corresponds to the sharp case of standard cascades. Correlations within the cascade process, and hence H will be increased with greater values of h.

- $S_{n,j}(\alpha, h) = \sum_{increments}^{\square} \left(\sum_{l \in portion\ of\ increments} c_l \right)^{\alpha}$ with n being the cascade level and j the position within the series. This quantity is different for each time step because the moving window does not always start on the same position within a portion of an increment.

  With these notations and using Eq. 7, one can easily obtain:

$$\left\langle a_{n,j}^{q} \right\rangle = \lambda_n^{\frac{C_1}{\alpha-1} S_{n,j}(\alpha,h)(q^{\alpha}-q)} \qquad (14)$$

Finally, the scaling behaviour of the process A must be studied. In general $S_{n,j}(\alpha, h)$ depends on both the cascade step n and the position within the series j. However scaling behavior corresponds to an average one, where all the possible values of j should be accounted for, which means that the quantity of interest is actually

$S_n^{1D}(\alpha,h)=\left(\sum_{k=¿}^{s_n}\left(S_{c,k}(\alpha,h)\right)\right)/s_n$. The '1' refers to dimension of the embedding space which is equal to 1 here. It turns out that the quantity $S_n^{1D}(\alpha,h)$ rapidly (i.e. after few cascades steps) converges toward an asymptotic value denoted $S_{\square}^{1D}(\alpha,h)$ (see Gires et al. 2020 for more details). Because of this small change with the cascade step, it is needed to implement two additional steps and average the final values over 4 successive steps to generate the wanted field (again see Gires et al. 2020 for more explanations). The behaviour of $S_{\square}^{1D}(\alpha,h)$ as a function of α or h is displayed in Fig. 2.

Given the previous computations, it is possible to write the scaling moment function $K_{blunt}(q)$ of the process A as :

$$K_{blunt(q)}=\frac{C_1 S^{1D}(\alpha,h)}{\alpha-1}\left(q^{\alpha}-q\right)=S^{1D}(\alpha,h)K(q) \tag{15}$$

which yields simple relations between the UM parameters of the blunt process and the ones from the standard process:

$$\begin{array}{lll}\alpha_{blunt} & ¿ & \alpha \\ C_{1,blunt} & ¿ & S^{1D}(\alpha,h)C_1\end{array} \tag{16}$$

It can be noted that when $h=0$, which corresponds to the sharp case of standard cascades, $S^{1D}(\alpha,h)$ meaning that common Eq. 3 is found back.

Brief discussion on the renormalization of the increments

Before developing the extension to 3D fields, the issue of renormalisation should be discussed, i.e. the denominator in Eq. 13. Indeed, a slight small difference in introduced here with regards to Gires et al. (2020). In the latter, $S_n^{1D}(\alpha,h)$ was used and not $S_{n,j}^{\square}(\alpha,h)$ as done in this paper.

The issue is illustrated in Fig. 3 where the average for each time step over 10 000 realisations in various configuration is displayed. Simulations of length 256 (i.e. 10 cascade steps followed by an average over the two last ones) with $\alpha = 1.8$, $C_1 = 0.2$ and $h = 1$ as input parameters are used. Similar patterns are retrieved for other input parameters. The series in black corresponds to standard discrete cascades and exhibits values always close to one, which is what is expected. With the previous normalization (i.e. with $S_n^{1D}(\alpha, h)$ in the denominator of Eq. 13), which is displayed in red, a clear problem on both sides of the series is visible with average values significantly increasing. This is due to the fact that the formula does not take into account side effects properly with unique normalisation independent of the position within the time series. Given that in Gires et al. (2020), only the middle portions of the simulated series were used, the issue was not addressed. In this paper, the whole fields will be used, since we aim at generating the missing halves and that we are working in a 3D framework which is more computationally expensive. Hence, it needs to be handled. The normalisation is therefore changed and tailored to the actual weighting coefficients used in the geometric average of the adjacent increments for each given time step. The corresponding outcome of this strategy is displayed in blue in Fig. 3. Value continuously close to one and following in a slightly dampened way the ones of the standard case (i.e. the black curve) are found, which highlights the validity of this strategy.

Extension to 2D and 3D: methodology and validation

The extension of the blunt process in 2D is straightforward and was actually already introduced in Gires et al. (2020). It simply consists in generating sharp increments with a discrete cascade process and then doing the geometric interpolation over the adjacent increments with the moving window successively on each line and then row. In a

similar way as in 1D, a $S^{2D}(\alpha,h)$ can be defined and it is easy to show that it is equal to $S^{1D}(\alpha,h)$ raised to the power 2 :

$$S^{2D}(\alpha,h)=\left[S^{1D}(\alpha,h)\right]^2 \qquad (17)$$

It is displayed along with $S^{1D}(\alpha,h)$ in Fig. 2.

The extension in 3D, i.e. space-time processes, is also theoretically not complicated, except for the fact that a scaling anisotropy coefficient (H_t) between space and time should be accounted for (Deidda 2000, Gires et al. 2011). More precisely, it means that when the spatial scale is changed by a ratio of λ_{xy}, the temporal scale should be changed by a ratio of $\lambda_t=\lambda_{xy}^{1-H_t}$. By combining Kolmogorov's formulation (Kolmogorov 1962) and the scale invariance of Navier-Stokes equations, one can show that $H_t=1/3$ is expected (Marsan et al. 1996). Biaou et al. (2005) initially suggested to use $\lambda_{xy}=3$ and $\lambda_t=2$, which are integer ratios enabling to remain close to the theoretical expectations given that $3^{1-1/3}\approx 2.08$. Such combination of ratios already reused in Gires et al. (2014a, 2014b) is implemented here to generate the sharp increments and the standard cascade process. Hence, at each step of a discrete cascade process, a parent structure is divided into 18 (=3 x 3 x 2) sub-structures.

Once the sharp increments are simulated, the same process of geometric interpolation as the one described in section 2.2 for 1D fields is implemented successively in the two spatial directions (taking $\lambda_1=\lambda_{xy}=3$) and then in the temporal direction (taking $\lambda_1=\lambda_t=2$). Similarly, this yields to a correction coefficient $S^{3D}(\alpha,h)$ for the simulated C_1 defined as :

$$S^{3D}(\alpha,h)=\left[S_{xy}^{1D}(\alpha,h)\right]^2 S_t^{1D}(\alpha,h) \qquad (18)$$

Behaviour of $S^{3D}(\alpha,h)$ as a function of α or h is displayed in Fig. 2. Similar patterns as in 1D or 2D are retrieved with values yielding stronger differences between the C_1 used as input and the one assessed from simulation.

Fig. 4 and Fig. 5 display the successive time steps of one realisation of a simulated UM space-time cascade process of final size 27 x 27 x 8 with $\alpha=1.7$, $C_1=0.4$ and $h=2$ used as input parameters. The former corresponds to the standard case while the latter is the blunt process with the same sharp increments to enable relevant comparison. The effect of the blunting that removes unrealistic square structure and sharp transitions is clearly visible.

The last step consists in checking that the simulated fields exhibit the correct expected multifractal behaviour. It is done by performing a space-time DTM analysis (i.e. fields are upscaled by a ratio of $\lambda_{xy}=2$ and $\lambda_t=2$ at each cascade steps). An illustration is displayed in Fig. 6 for an ensemble analysis of 100 independent realisations for$\alpha=1.6$, $C_1=0.2$ and $h=1$. Fig. 6 shows that an excellent scaling behaviour is found with r^2 coefficients greater than 0.99 (Fig. 6.a) and expected shape with a visible linear portion on the UM parameters determination curve (Fig. 6.b). Similar behaviour is found for other input parameters.

In order to check if simulated UM parameters are in agreement with expectations, i.e. that same α are retrieved and that C_1 assessed is simply the one input multiplied by $S_{\square}^{3D}(\alpha,h)$, all the possible combinations of UM parameters for $\alpha\subset[0.2,0.4,0.6,1,1.2,1.4,1.6,1.8]$ and $C_1\subset[0.1,0.2,0.3,0.4,0.5]$ for $h=1$ are tested. Ensembles of 100 realisations of independent fields of final size 27 x 27 x 8 are simulated and then analysed. Assessed UM parameters are displayed in Fig. 7 along with theoretical expectations (solid lines) for standard discrete fields. The input

parameters are properly retrieved on the simulated fields, which is expected. Same results for the blunt process are shown in Fig. 8. Results are more contrasted. Same α parameter as the input one are almost retrieved for $\alpha > 1$ (Fig. 8.a). The expected decreasing trend for C_1 as a function of α_{input} is retrieved but the differences between simulation outputs and expectations tend to significantly increase for $\alpha < 1$ (Fig. 8.a). Hence it can be said that theoretical expectations are retrieved for great values of α (>1) and small values of C_1 (<0.3-0.4). Typical UM parameters for rainfall fall within this range of values. For smaller values of α and greater values of C_1, some discrepancies appear. It should be reminded here that fields with $\alpha < 1$ are intrinsically harder to simulate, notably because for example their mean is not theoretically defined. Also, only 3 (or more precisely 5-2) cascade steps are used, meaning that it may not be enough to ensure that the expected multifractal behaviour is fully developed.

A new algorithm to generate a missing half of a multifractal field

The purpose of this section is to describe a new algorithm to generate the missing half of a multifractal field assuming that it is generated through a 'blunt discrete cascade process'. The studied field is also assumed to be normalized to one. The methodology is explained in 1D with the corresponding illustration but the same process can actually be implemented in 2D and 3D using the same generalization as presented in section 2.4.

A scheme of the situation is displayed in Fig. 9. The available data which corresponds to the input of the algorithm consists in a series which is shown in blue on the left. The data to be guessed which corresponds to the output of the algorithm (in green) is the follow up of the initial series. The field is assumed to be generated through a blunt discrete cascade, meaning that it is fully determined by its underlying sharp increments. Hence the whole purpose of this algorithm consists in determining these

increments while ensuring that the field has the required multifractal properties and has values as close as possible to the actual ones on the available portion. To summarize, a portion of the increments is stochastically simulated (red rectangles) and the rest is deterministically reconstructed through an iterative process (purple rectangles). Given that half of the data is known, it is a rather natural choice to look for deterministically reconstructing half of the increments and stochastically generating the others. Other options, notably for the increments close to the transition could be tested in future improvements of the algorithm. Before going on, it should be mentioned that the overall concept of deterministically reconstructing a portion of the field and stochastically simulating the other has been well used in previous work on forecasting (Marsan et al. 1996, Schertzer and Lovejoy 2004, Macor 2007, Macor et al. 2007) or sparse network measurements (Salvadori et al. 2000, Tchiguirinskaia et al. 2004, Paz et al. 2020). It relied on the use of continuous UM cascades. Here we are keen to remain within the framework of discrete cascades for the reasons mentioned in the introduction.

Let us now describe in detail the algorithm which is made of two successive steps. In the first step, an initial guess of the increments is computed. The ones corresponding more to the portion to be guessed (i.e. in red in Fig. 9) are stochastically simulated using Eq. 6 with given α and C_1 (computed from the available data) and set to a definitive value. The others (in purple in Fig. 9) are simply set to one divided by the average renormalization factor at each cascade step. The purpose is to ensure that the blunt field will have values close to its average value of one for this portion.

The second step consists in an iterative process to tune the 'purple' increments so that the blunting of these sharp increments yields the wanted value on the known portion of the series (in blue in Fig. 9). This step of the algorithm is actually the trickiest

and various heuristic approaches have been tested. The one yielding the best results is the following:

- A first estimate of the blunt simulation (denoted $¿_{blunt}$) is computed from this first guess of sharp increments. At this first iteration, it will obviously be quite far from the known data.

- The ratio of the data to $¿_{blunt}$ ($Ratio = data / ¿_{blunt}$) is computed. For the second half of the series, this *Ratio* is simply set to one. Since the data is normalized to one and the sharp increments were initially chosen to ensure that $¿_{blunt}$ is close to one, the average of *Ratio* will be close to one which is what we want for the next step.

- The sharp increments yielding to this field (*Ratio*) then are assessed. This is done by using at each scale (or cascade step) the same matrices as in the blunting process to obtain a 'smoothed' field. Taking the ratio between two successive cascade steps then yields to the dressed blunt increments. The sharp ones are then assessed by taking the average at the corresponding scale. This approach assumes that the field is normalized to one. Given the choice of initial increments, this is approximately the case. However, a small correction is implemented with the total average of the field, by taking it and distributing it uniformly over all the scales (to ensure that the initial average is retrieved).

- The purple sharp increments are then updated by multiplying the current ones with the 'dressed ones from *Ratio* '.

- Finally, the process is repeated, i.e. a new blunt simulation is computed from these updated sharp increments, leading to a new ratio enabling a new update of

sharp increments.

Few iterations of the process are displayed for an example in Fig. 10 for the successive simulations and in Fig. 11 for the ratios. The initial series which has a length of 128 time steps is in black in Fig. 10. $\alpha = 1.6$, $C_1 = 0.2$ (actually divided by $S_{\square}^{1D}(\alpha, h)$ to retrieve the correct value at the end) and $h = 2$ are used. It can be seen that after very few iterations, the *Ratio* is becoming always close to one (except for time steps with very small value) and the simulation close to the initial data which is what we wanted. In the lower part of Fig. 10, the transition between the initial data and the stochastically generated second half is visible. It can be seen that value at step 127 is strongly increased to reach the one of the data, which also increases the values of the next steps. The corresponding increments (both sharp and blunt) are displayed in Fig. 12. The blunting process enables a smooth transition at all scales between the known and generated portion of the field. It can also be seen that the fluctuations of the increments on the known portion of the data (i.e. the ones obtained by dressing the field) are smaller than the ones of the stochastically simulated portion, which is a behaviour to be expected. One can note (this is visible on the last cascade steps) that sharp increments have a smaller average value on the dressed part than the simulated one (typically 0.85 vs. 1), while the same average of ≈ 1 is retrieved on the blunt increments. This is due to the fact the renormalization of the blunt increments assumes that sharp ones are distributed as UM ones with given α and C_1. This is the case for the simulated ones but not exactly for the dressed ones.

Before implementing the algorithm in next section, two remarks should be made. First, in the developed process, the values of the deterministically reconstructed increments actually depend on the value of the stochastically simulated ones. This is done to ensure a smooth realistic transition at all cascade steps between the known and

generated portion of the field. Second, the process is stochastic, meaning that ensemble of realistic realisations can be simulated enabling to compute quantiles.

Implementation and validation of the algorithm

In this section, we implement the new algorithm to generate a missing half of fields in 1D, 2D and 3D to illustrate and validate the process. Rainfall disdrometer data is used in 1D, weather radar rainfall estimates map is used in 2D and numerical simulations in 3D.

In 1D with rainfall disdrometers time series

In this subsection, the algorithm is tested with the help of a rainfall time series that was collected on 30 May 2016 by a OTT Parsivel^2 disdrometer (Battaglia et al. 2010, OTT 2014) located on the roof of the Carnot building of the Ecole des Ponts ParisTech campus. It is part of the TARANIS observatory of the Fresnel Platform of École des Ponts ParisTech (https://hmco.enpc.fr/portfolio-archive/fresnel-platform/). A series with 1 min time steps lasting 256 min is used here. It is shown in Fig. 14 in black. Only the first half of the data is used as input for the algorithm, while the second half is only displayed for validation purposes. Full presentation and associated references of the data can be found in Gires et al. (2018) which describes the measurement campaign. A UM analysis on the whole series showed that it exhibited an excellent scaling behaviour with $\alpha = 1.53$, $C_1 = 0.21$ and $H = 0.62$ (with a spectral slope $\beta = 1.88$). Given the high value of β, the TM and DTM analysis was carried out on the fluctuations of the field in order to ensure that a conservative field is studied (Lavallée et al. 1993). Before going on, it should be stressed that a similar analysis was carried out on the two halves independently and highlighted some differences. Indeed, we find $\alpha = 1.85$, $C_1 = 0.30$ and $H = 0.64$ (with a spectral slope $\beta = 1.73$) for the first half and $\alpha = 1.30$, $C_1 = 0.20$ and

$H = 0.67$ (with a spectral slope $\beta = 2.03$) for the second half with a slightly worse scaling. The determination coefficient r^2 in the TM analysis is of 0.93 for the second half while it is of 0.98 for the first half, and of 0.95 considering the whole series. TM curve for the first half is displayed in Fig. 13 for illustration. Scaling properties are ensemble ones, so one should be cautious while interpreting results for single short series. However, it should be mentioned that, currently, potential variations of UM parameters between the first and second half are not accounted for and values on the whole time series with $h = 6$ are used. The value of C_1 is actually divided by $S_{\square}^{1D}(\alpha, h)$ to retrieve the correct value at the end. An ensemble of 1000 realisations was generated. One sample is displayed in red in Fig. 14.

First, a UM analysis on the simulated portion (i.e. the second half) was carried out. It is displayed in Fig. 15. It can be seen that an excellent scaling behaviour is retrieved with $\alpha = 1.47$, $C_1 = 0.18$ and $\beta = 1.61$. The UM parameters are close to the ones used as inputs. The spectral slope is slightly smaller (-0.17) than the one of the original series. Despite this slight difference, the auto-correlation within the simulated series can be considered as similar to the expected one. Hence, the simulated portion of the field exhibits the expected (i.e. the one used as input) multifractal behaviour which is one of the wanted features for the developed algorithm. It should be reminded here that scaling behaviour encompasses statistics for all moments. Hence its preservation means that the scale dependence of commonly used statistics such as coefficient of variations, skewness or flatness are also preserved (Schertzer et al. 2010). Fig. 14 also displays the 5, 50, and 95 % quantiles which have been computed for each time step over the 1000 realisations. Through the analysis of the quantile curves, it can be seen that the influence of the 'known portion' of the initial data lasts few time steps (roughly 5 min). It can also

be seen that the immediate follow up of the series is well captured within the 90 % quantile margins. This confirms the relevancy of the developed algorithm.

In 2D with rainfall weather radar maps

In this sub-section, the new algorithm is tested to generate the missing half of a rainfall map measured on 16 September 2015 by a X-band radar operated by Ecole des Ponts ParisTech on its campus. The pixel size of the data provided by the radar is 250 m x 250 m, and the data corresponding to the average rain rate over a 3 min and 40 s time step that started at 09:06 UTC is used. The 64 x 128 pixels used in the analysis are displayed on Fig. 16 (top-left). Actually, only the left half (i.e. an area of 64 x 64 pixels) is used as input, while the other half is shown only for comparison purposes with the algorithm's outputs. A multifractal analysis, implemented on the 64 x 128 initial area (considering to samples of size 64 x 64), showed that the field exhibited a very good multifractal behaviour with $\alpha = 1.97$, $C_1 = 0.096$, $H = 0.57$ (with a spectral slope $\beta = 1.95$). Given the elevated value of H the analysis was implemented on the fluctuations. As for the 1D case, it should be mentioned that both portion of the field exhibit slightly different values of UM parameters. Indeed we find $\alpha = 2.09$ (which is slightly greater than the maximum value of 2, indicating that simply taking the fluctuation may not be sufficient to retrieve the conservative underlying field), $C_1 = 0.10$, $H = 0.62$ (with a spectral slope $\beta = 2.03$) for the left portion; and $\alpha = 1.58$, $C_1 = 0.089$, $H = 0.56$ (with a spectral slope $\beta = 1.97$). The parameters (with the standard correction for C_1) obtained by analysing both portions along with $h = 6$ are used for the stochastic generation of the missing half. 100 realisations are generated

Fig. 16 displays two specific realisations where the smooth transition between the initial data (left) and stochastic generation (right) is visible. It should be stressed that

it is more visible for the first sample than for the second one. It also hints at a possible need to improve the transition in further versions of the algorithm which appears to be quite sensitive to the renormalization of the first guess of increments. In general, it can also be seen that the generated halves exhibit similar pattern as the initial data, which was expected since same UM parameters are used. More precisely, as for the 1D case, an ensemble UM analysis was performed on the set of 100 samples for the generated portion of the field. Similar curves as in Fig. 15 are obtained and therefore not shown. $\alpha = 1.84$, $C_1 = 0.10$ and $\beta = 1.62$ are found which is close to the input values. There is a slight underestimation of the spectral slope (more pronounced than in the 1D case) resulting in slighter auto-correlation than in the original field. The 5, 50 and 95 % quantiles computed for each pixel over the 100 realisations are displayed on the left part of Fig. 16. Same comments as for the case in 1D can be made, i.e. the influence of the known data remains strong for only few pixels and the actual data for the generated half falls within the 90% quantiles margin of the stochastically simulated missing halves.

In 3D with numerical simulations

Only numerical simulations are used to illustrate the potential use of the algorithm to generate the following time steps of a space-time process. More precisely, a space time field of size 27 x 27 x 8 is generated with the help of a blunt discrete cascade process (see section 2.4) and the algorithm is implemented to generate a realistic potential realisation of the next 8 time steps.

Fig. 17 displays an example obtained with $\alpha = 1.7$, $C_1 = 0.9$ (meaning that the actual C_1 of the final field is 0.083, see Eq. 18), and $h = 4$ as input. The first 8 time steps are obtained from a simulation, and the next ones (i.e. from time step 8 to 15) are obtained through the new algorithm using only the final field (i.e. not the increments) as

input. A rather soft transition is visible and corresponds to the wanted feature, along with the fact that the two portions of the fields exhibit the same multifractal behaviour.

Conclusion

In this paper we first suggested an extension to space-time processes of the previously developed blunt extension of UM discrete cascades (Gires et al. 2020). This model was initially suggested to lessen the lack of stationarity of discrete random multiplicative cascades which is one of their main limitations. At each cascade step of such process, a parent structure is divided into substructures and the value affected to a substructure is the parent's one multiplied by a random increment. Hence the process is actually determined by the succession of all the increments at each cascade steps. The blunt extension of discrete cascades consists in introducing the final resolution at each cascade step and geometrically interpolating the increments in order to smooth the transition between them. The size of the moving window over which the interpolation is implemented is defined by a parameter h which corresponds to the number of multiplicative increments at a given cascade level that are influencing the blunt ones.

The model was initially developed in 1D and 2D, and an extension to space-time processes is introduced here, where two dimension corresponds to space and one to time. A scaling anisotropy between space and time is accounted for as commonly done (Biaou et al. 2005). The extension required to solve a renormalization issue affecting mainly the sides of the numerical simulations. It is established that the generated fields should also exhibit a multifractal behaviour with the same multifractal index α and mean intermittency codimension C_1 changed to $C_1 S^d(\alpha, h)$. Such expectations are numerically confirmed only on a limited range of UM parameters (typically for $\alpha > 1$ and $C_1 < 0.3-0.4$). For other ranges of parameters some strong deviations are noted,

which limits potential applications. It should be noted that common rainfall UM parameters ($1.5<\alpha<2$ and $0.05<C_1<0.2$) fall within the range of validity of the developed blunt model.

The second step of this paper consists in developing a new algorithm to generate the missing half of multifractal fields in 1D, 2D or 3D. The overall idea was to remain in the rather simple and intuitive framework of discrete cascades. Indeed, despite some drastic limitations which have been pointed out since Schertzer et al. (1987) and are acknowledged by Gires et al. (2020), discrete cascades process enables to reproduce complex patterns exhibiting extreme variability and intermittency over a wide range of spatio-temporal scales. It is done by computing a set of increments that once blunted yield a field with the expected value on the available data and the wanted scaling properties. This is achieved by stochastically generating half of the increments and deterministically reconstructing step by step the others. Such method intrinsically follows a scale invariant approach throughout the whole process, although only over discrete scales. Indeed, the shift from the deterministically reconstructed part to the stochastically simulated one is handled in the same way at all the scales, defined by the (discrete) cascade steps, through the 'blunting'. Such behaviour is partly consistent with the expected behaviour inherited from the (continuous) scale symmetries of the underlying Navier-Stokes equations. This process enables to generate not only a single deterministic guess but also ensembles of realistic guesses of the missing half which can be used later for uncertainty quantification. Finally, it should be stressed that the developed approach is parsimonious since it relies only on the three UM parameters α and C_1, and H (represented by h in the process). The algorithm is then implemented and validated with actual rainfall with disdrometer time series and rainfall maps. It is finally implemented in space-time with numerical simulations as a proof of concept.

There are still some limitations to the developed algorithm. Indeed, as pointed out in section 4, it appears that the algorithm is quite sensitive to how the reconstruction of the so-called known part of the increments is handled. Currently, a rather natural approach is implemented and further sensitivity analysis should be carried out. Another issue that should be studied deeper is the potential variations of underlying UM parameters between the two halves of the field. Indeed, currently average values are used but it was shown that strong variations may exist. New studies on the variations of these parameters in both space and time should be carried out. An important feature of rainfall fields which has not been addressed yet in the blunt extension framework, and should be in future, is spatial anisotropy. In order to achieve this, the approaches discussed by Seed et al. (2003) and Niemi et al. (2014) could be helpful. Additionally, improving the simulations of the zeros of the rainfall fields could be beneficial (see Gires et al. 2013 for a complete discussion and lead of developments). Such application to space-time processes is actually a first step toward the nowcasting of geophysical fields such as rainfall. It enables to account for the increase or decrease of rainfall cells. However, it does not address advection which should be handled separately and is outside the scope of this paper. Accounting for advection will enable comparison with currently available rainfall nowcasting algorithms.

Acknowledgements

The authors gratefully acknowledge partial financial support from the Chair “Hydrology for Resilient Cities” (endowed by Veolia) of Ecole des Ponts ParisTech, the Île-de-France region RadX@IdF Project, and the ANR JCJC RW-Turb project (ANR-19-CE05-0022-01)

References

Battaglia, A., *et al*., 2010. PARSIVEL snow observations: a critical assessment. *Journal of Atmospheric and Oceanic Technology*, 27 (2), 333–344. doi:10.1175/2009JTECHA1332.1

Ben Aissia, M.-A., Chebana, F. and Ouarda, T., 2017. Multivariate missing data in hydrology – a review and applications. *Advances in Water Resources*, 110, 299-309. Doi: https://doi.org/10.1016/j.advwatres.2017.10.002

Biaou, A. et al., 2003. Fractals, multifractals et prévision des précipitations. *Sud Sciences et Technologies*, 10, 10-15.

Bowler, N., Pierce, C. and Seed, A., 2006. STEPS: A probabilistic precipitation forecasting scheme which merges an extrapolation nowcastwith downscaled NWP. *Quarterly Journal of the Royal Meteorological Society*, 132(620):2127–2155. doi: 10.1256/qj.04.100

Chambers, J. M., Mallows, C. L. and Stuck, B. W., 1976. Method for simulating stable random-variables. *Journal of the American Statistical Association*, 71, 340-344. doi:10.1080/01621459.1976.10480344

Deidda, R., 2000. Rainfall downscaling in a space-time multifractal framework. *Water Resources Research*, 36,1779-1794. doi:10.1029/2000WR900038

Frisch, U., Sulem, P.-L. and Nelkin, M., 1978. A simple dynamical model of intermittent fully developed turbulence. *Journal of Fluid Mechanics*, 87 (4), 719-736. doi: 10.1017/S0022112078001846.

Garciarena, U. and Santana, R., 2017. An extensive analysis of the interaction between missing data types, imputation methods, and supervised classifiers. *Expert Systems with Applications*, 89, 52 – 65. doi: 10.1016/j.eswa.2017.07.026

Gaume, E., Mouhous, N. and Andrieu, H., 2007. Rainfall stochastic disaggregation models: Calibration and validation of a multiplicative cascade model. *Advances in Water Resources*, 30(5),1301-1319. doi: 10.1016/j.advwatres.2006.11.007.

Gires, A., Tchiguirinskaia, I. and Schertzer, D., 2018. Two months of disdrometer data in the Paris area. *Earth System Science Data*, 10(2), 941-950. doi: 10.5194/essd-10-941-2018.

Gires, A. et al., 2011. Analyses multifractales et spatio-temporelles des precipitations du modèle Meso-NH et des données radar. Hydrological Sciences Journal, 56(3), 380–396. doi: 10.1080/02626667.2011.564174

Gires, A. et al., 2013. Development and analysis of a simple model to represent the zero rainfall in a universal multifractal framework. *Nonlinear Processes in Geophysics*, 20(3), 343-356. doi: 10.5194/npg-20-343-2013.

Gires, A. et al., 2014. Impacts of small scale rainfall variability in urban areas: a case study with 1d and 1d/2d hydrological models in a multifractal framework. *Urban Water Journal*, doi: 10.1080/1573062X.2014.923917.

Gires, A., Tchiguirinskaia, I. and Schertzer, D., 2021. Infilling missing data of binary geophysical fields using scale invariant properties through an application to imperviousness in urban areas. *Hydrological Sciences Journal*, 66(7):1197–1210, 2021. doi: 10.1080/02626667.2021.1925121

Gires, A. et al., 2014. Influence of small scale rainfall variability on standard comparison tools between radar and rain gauge data. *Atmospheric Research*, 138(0):125–138. doi: 10.1016/j.atmosres.2013.11.008

Gupta, V.K. and Waymire, E., 1993. A statistical analysis of mesoscale rainfall as a random cascade. *Journal of Applied Meteorology*, 32, 251–267. doi:10.1175/1520-0450(1993)032<0251:ASAOMR>2.0.CO;2

Hubert, P., 2001. Multifractals as a tool to overcome scale problems in hydrology. Hydrological Sciences Journal, 46 (6), 897–905. doi:10.1080/02626660109492884

Kolmogorov, A.N., 1941. Local structure of turbulence in an incompressible liquid for very large Reynolds numbers. Proceedings of the USSR Academy of Sciences, 30, 299.

Kolmogorov, A.N., 1962. A refinement of previous hypotheses concerning the local structure of turbulence in viscous incompressible fluid at high Reynolds number. *J. Fluid. Mech.*, 13(1):82–85. doi: 10.1017/S0022112062000518

Lavallée, D., Lovejoy, S., and Ladoy, P., 1993. Nonlinear variability and landscape topography: analysis and simulation. In: L. de Cola and N. Lam, eds. Fractals in geography. Englewood Cliffs, NJ: Prentice-Hall, 171–205.

Licznar, P., Lomotowski, J., and Rupp, D.E., 2011. Random cascade driven rainfall disaggregation for urban hydrology: an evaluation of six models and a new generator. *Atmospheric Research*, 99 (3–4), 563–578. doi:10.1016/j.atmosres.2010.12.014

Macor, J. Développement de techniques de prévision de pluie basées sur lespropriétés multi-échelles des données radar et satellites. PhD thesis, Ecole Nationale des Ponts et Chaussées, Marne La vallée, 2007.

Macor, J., Schertzer, D. and Lovejoy, S., 2011. Multifractal Methods Applied to Rain Forecast Using Radar Data. *La Houille Blanche*, 4:92–98, 2007 doi. https://doi.org/10.1051/lhb/2011039

Marsan, D., Schertzer, D. and Lovejoy, S., 1996. Causal space-time multifractal processes: Predictability and forecasting of rain fields. *J. Geophys. Res.*, 101:26333–26346. doi: https://doi.org/10.1029/96JD01840

Menabde, M. and Sivapalan, M., 2000. Modeling of rainfall time series and extremes using bounded random cascades and Levy-stable distributions. *Water Resources Research*, 36 (11), 3293–3300. doi:10.1029/2000WR900197

Müller, H. and Haberlandt, U., 2018. Temporal rainfall disaggregation using a multiplicative cascade model for spatial application in urban hydrology. *Journal of Hydrology*, 556, 847–864. doi:10.1016/j.jhydrol.2016.01.031

Niemi, T.J., Kokkonen, T., and Seed, A., 2014. A simple and effective method for quantifying spatial anisotropy of time series of precipitation. *Water Resources Research*, 50 (7), 5906–5925. doi:10.1002/2013WR015190

Olsson., J., 1998. Evaluation of a scaling cascade model for temporal rainfall disaggregation. *Hydrology and Earth System Sciences*, 2 (1), 1930. doi:10.5194/hess-2-19-1998

OTT, 2014. Operating instructions, present weather sensor ott parsivel 2. Kempten, Germany: OTT.

Over, T.M. and Gupta, V.K., 1996. A space-time theory of mesoscale rainfall using random cascades. *Journal of Geophysical Research - Atmospheres*, 101 (D21), 26319–26331. doi:10.1029/96JD02033

Paz, I., et al., 2018. Multifractal comparison of reflectivity and polarimetric rainfall data from c- and x-band radars and respective hydrological responses of a complex catchment model. *Water* (Switzerland), 10 (3). doi: 10.3390/w10030269.

Rupp, D.E., et al., 2012. Multiplicative cascade models for spatial downscaling of rainfall: parameterization with rain gauge data. *Hydrology Earth System Sciences*, 16 (3), 671–684. doi:10.5194/hess-16-671-2012

Salvadori, G., Schertzer, D., and Lovejoy, S., 2000. Multifractal objective analysis: conditioning and interpolation. *Stochastic Environmental Research and Risk Analysis*, 15, 261–283. doi:10.1007/s004770100070.

Schertzer, D. and Lovejoy, S., 1987. Physical modelling and analysis of rain and clouds by anisotropic scaling and multiplicative processes. *Journal of Geophysical Research*, 92 (D8), 9693–9714. doi:10.1029/JD092iD08p09693.

Schertzer, D. and Lovejoy, S., 1997. Universal multifractals do exist!:comments. *Journal of Applied Meteorology*, 36 (9), 1296–1303. doi:10.1175/1520-0450(1997)036<1296:UMDECO>2.0.CO;2

Schertzer, D., Tchiguirinskaia, I., Lovejoy, S. and Hubert, P., 2010. No monsters, no miracles: in nonlinear sciences hydrology is not an outlier! *Hydrol. Sci. J.*, 55(6), 965–979. https://doi.org/10.1080/02626667.2010.505173

Schertzer, D. and Lovejoy, S., 2004. Space–time complexity and multifractal predictability. Physica A: Statistical Mechanics and its Applications, 338(1):173–186, 2004. Proceedings of the conference A Nonlinear World: the Real World, 2nd International Conference on Frontier Science.

Schertzer, D., Tchiguirinskaia, I, 2020. A century of turbulent cascades and the emergence of multifractal operators. *Earth and Space Science*, 7(3). doi: 10.1029/2019EA000608

Seed, A.W., 2003. A dynamic and spatial scaling approach to advection forecasting. Journal of Applied Meteorology, 42 (3), 381–388. doi:10.1175/1520-0450(2003)042<0381:ADASSA>2.0.CO;2

Tchiguirinskaia, I., et al. 2004. Multiscaling geophysics and sustainable development. Scales in Hydrology and Water Management, IAHS Publ., 287, 113–136.

Figures and captions:

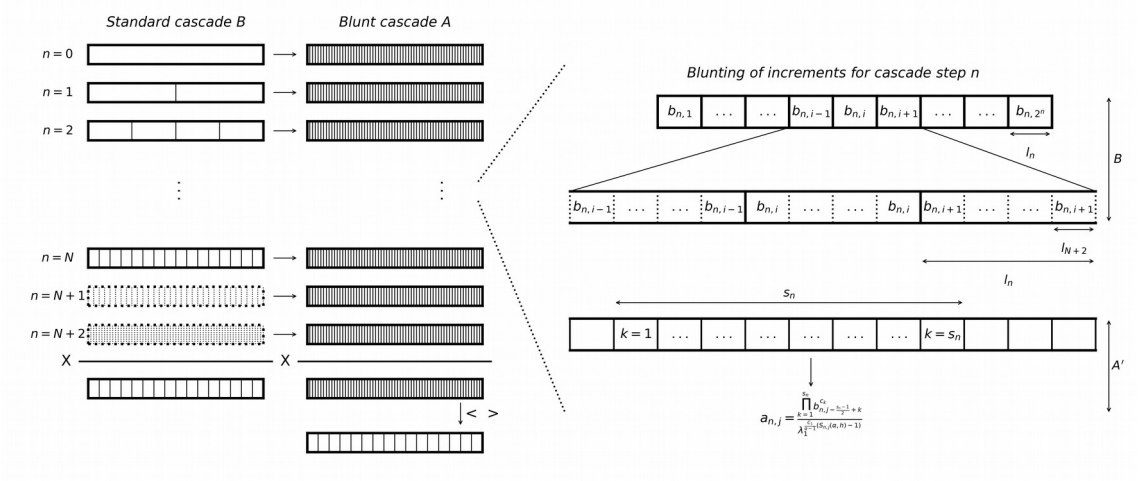

Figure 1: Schematic description of the generation of a blunt multiplicative cascade process *A* from a standard one *B*.

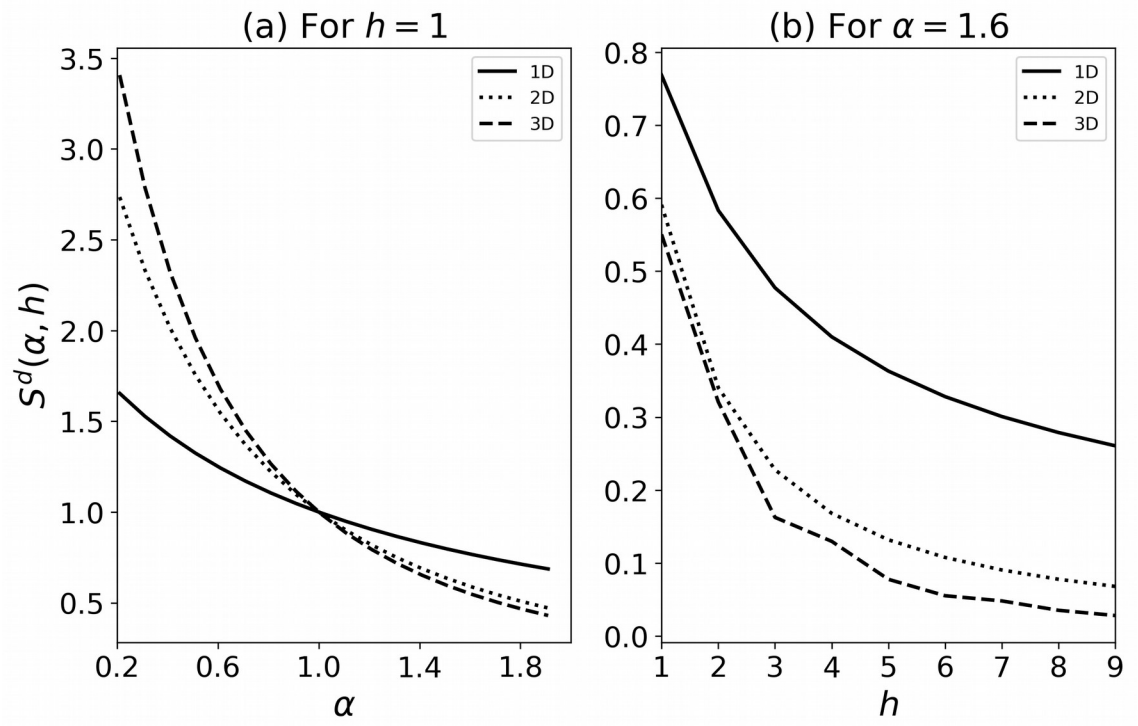

Figure 2: (a) $S^d(\alpha, h)$ vs. α for $h=1$ in 1D, 2D and 3D. (b) $S^d(\alpha, h)$ vs.h for $\alpha=1.6$ in 1D, 2D and 3D.

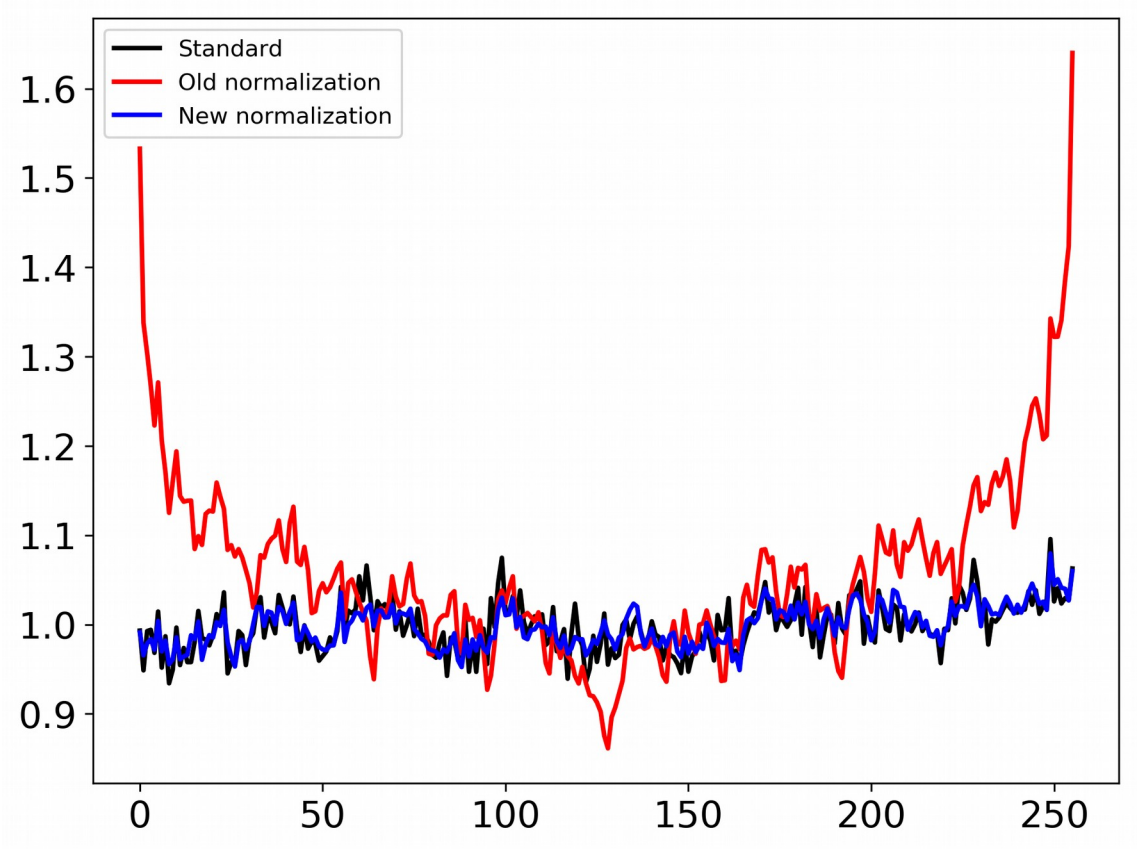

Figure 3: Time series of the average over 10 000 realisations of standard discrete cascades (in black) along with same computation for blunt process with the old (in red) and new normalization (in blue). $\alpha = 1.8$, $C_1 = 0.2$ and $h = 1$ are used as input parameters. 256 long times series are simulated.

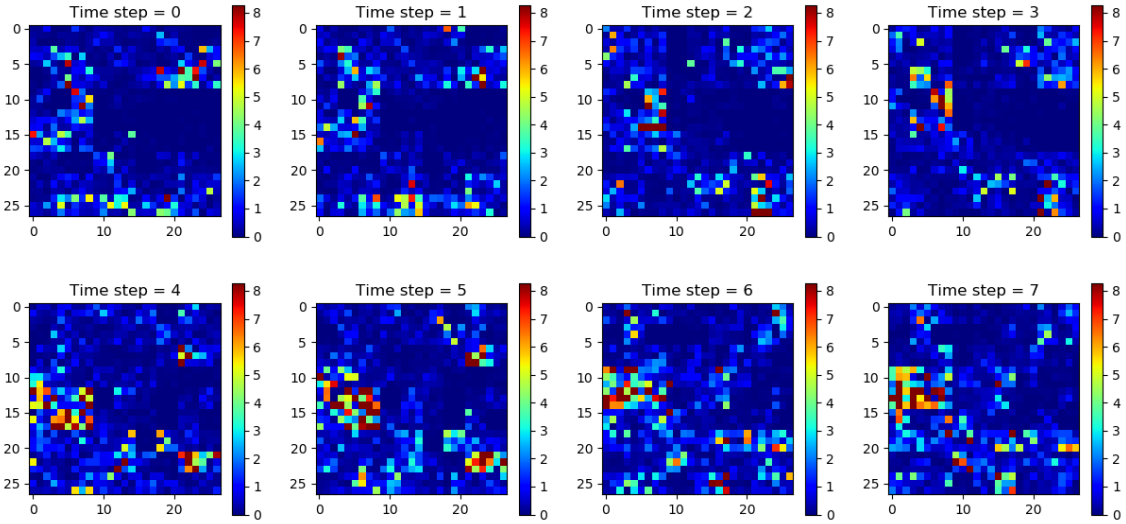

Figure 4: Display of the successive time steps of one realisation of a simulated standard space-time discrete cascade process of final size 27 x 27 x 8 with $\alpha = 1.7$, $C_1 = 0.4$ used as input parameters.

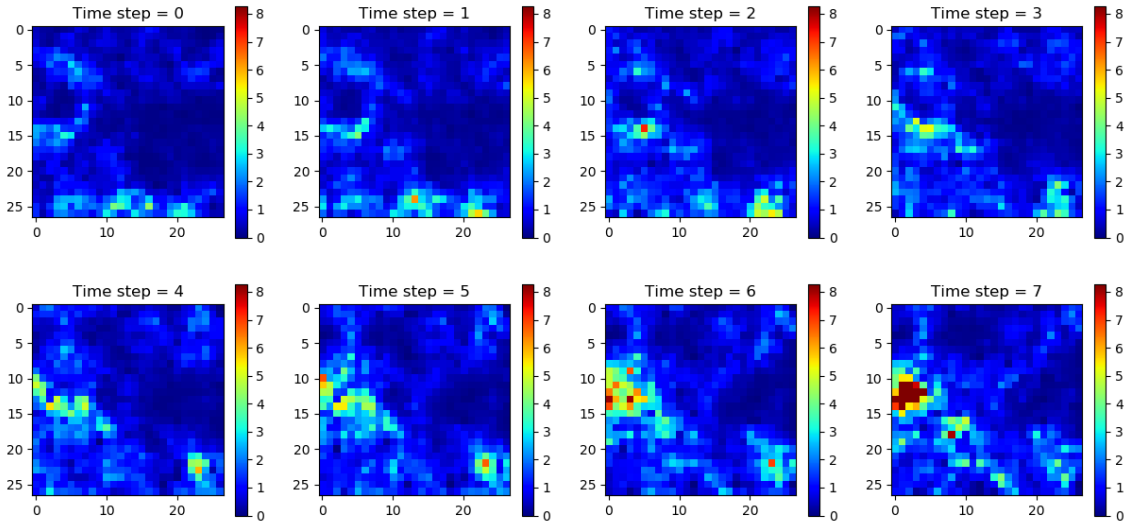

Figure 5: Same as Fig. 4 for the corresponding blunt process with $h = 2$.

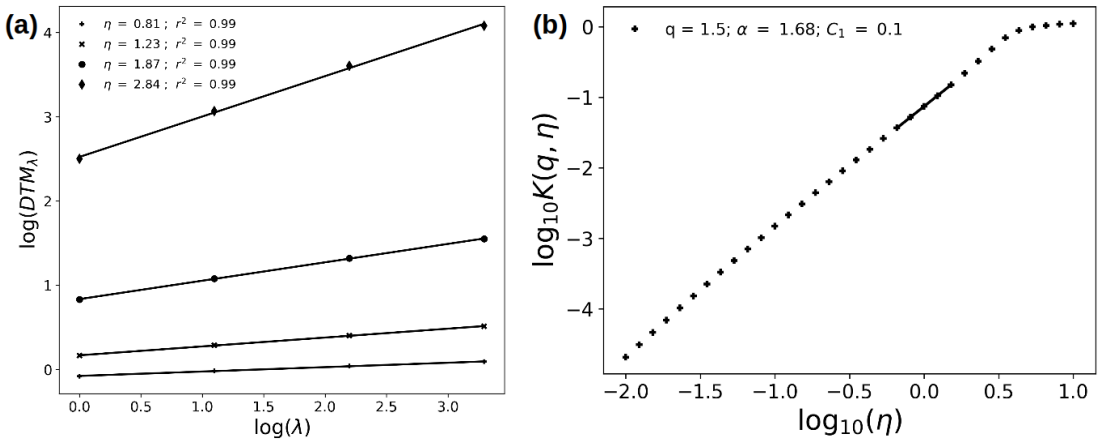

Figure 6: Space-time multifractal analysis of 100 realisations of the space-time blunt cascade process A with $\alpha=1.6$, $C_1=0.2$ and $h=1$. (a) Scaling in the DTM (Eq. 4 in log-log) and (b) UM parameters determination curve in the DTM analysis (Eq. 5 in log-log).

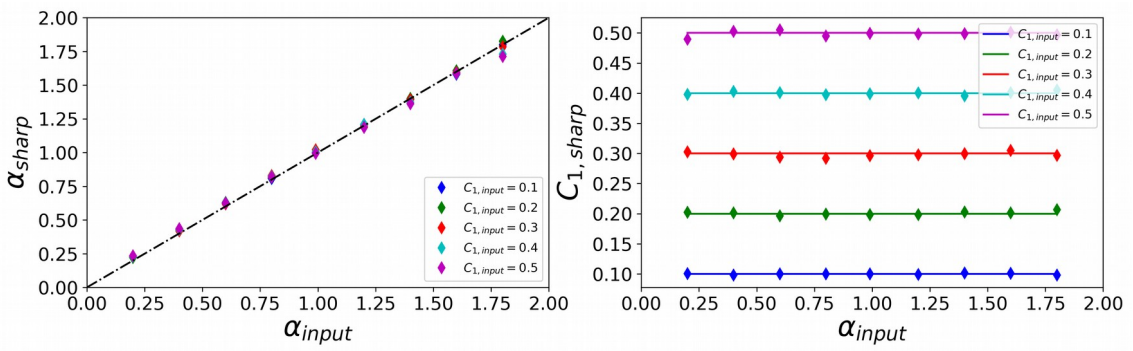

Figure 7: Comparison for space-time fields (ensembles of 100 3D realizations of size 27 x 27 x 8) of UM parameters estimated on numerical simulations for standard UM discrete cascade process with regard to parameters input to the simulations.

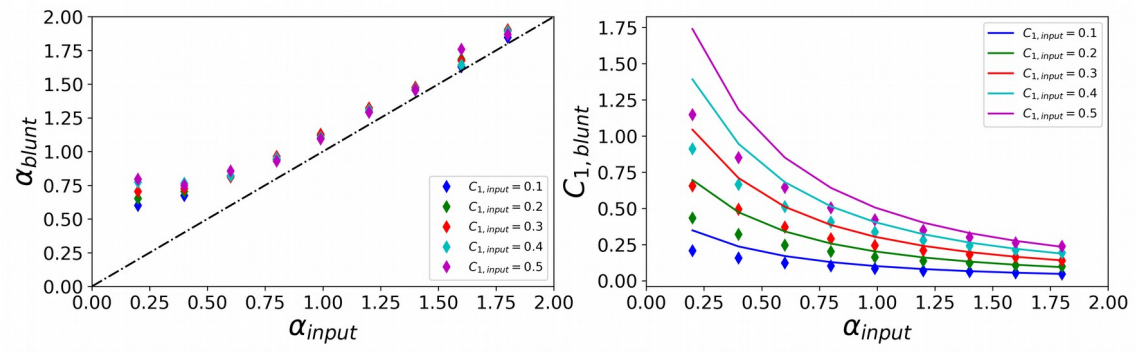

Figure 8: Same as in Fig. 7 but for blunt simulations. $h=1$ for the results displayed in this figure.

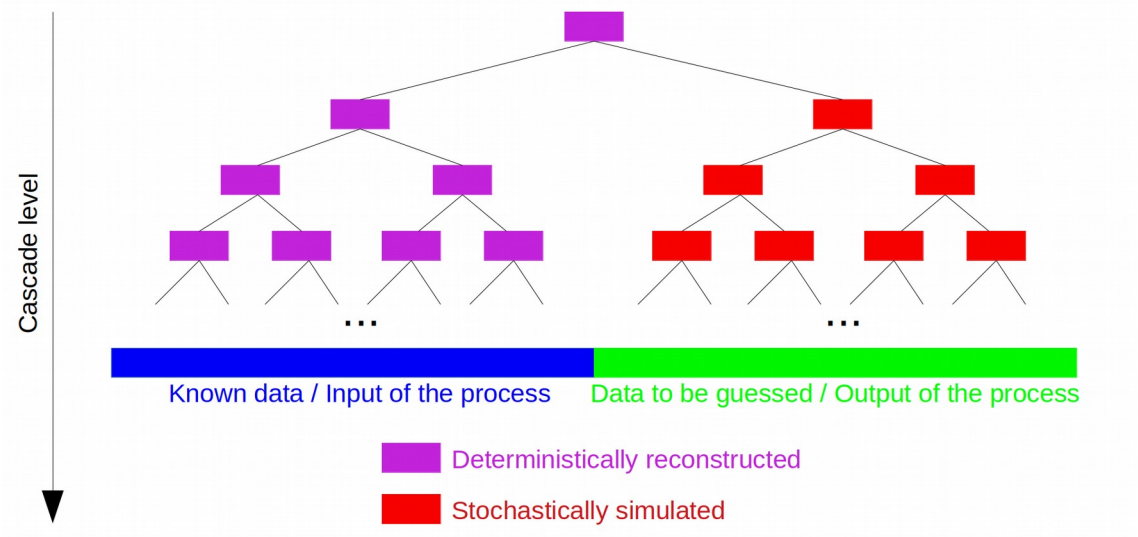

Figure 9: Scheme illustrating the newly developed process to generate a missing half of a multifractal field.

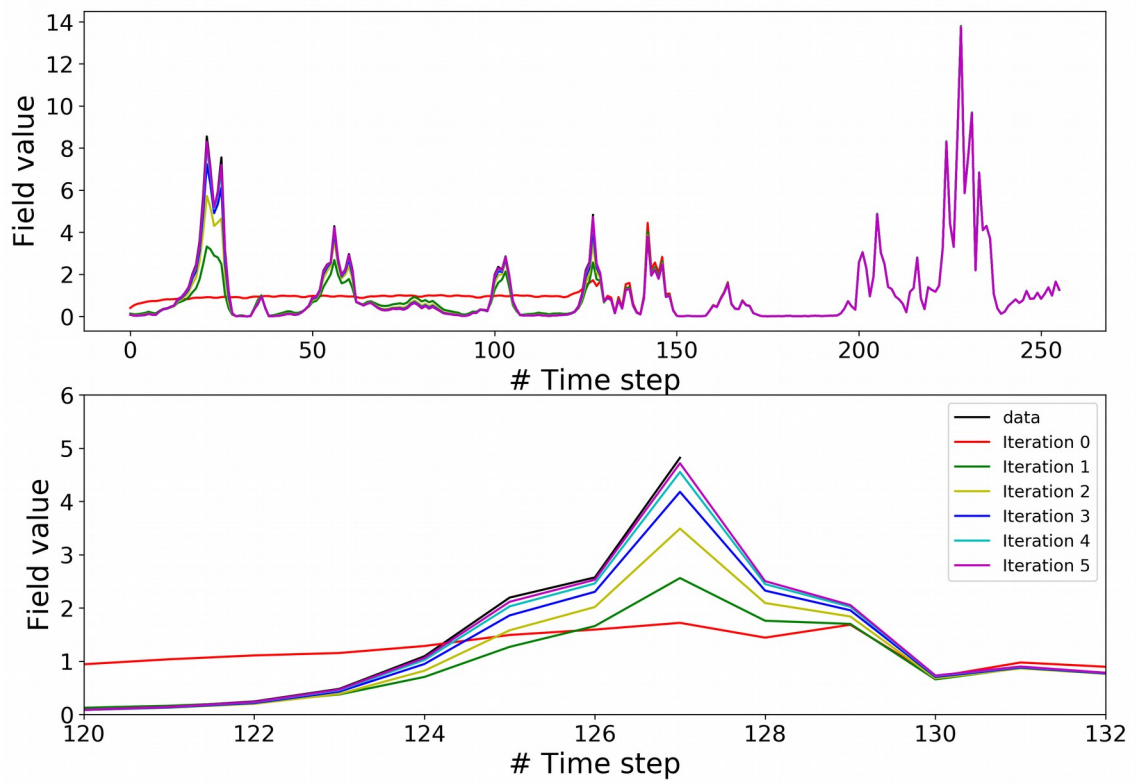

Figure 10: Illustration of the successive iterations of the process enabling to simulate a realistic follow-up of the initial series (of length 128) which is displayed in black. The lower part is simply a zoom of the upper one during the transition between the initial data and the stochastically generated second half.

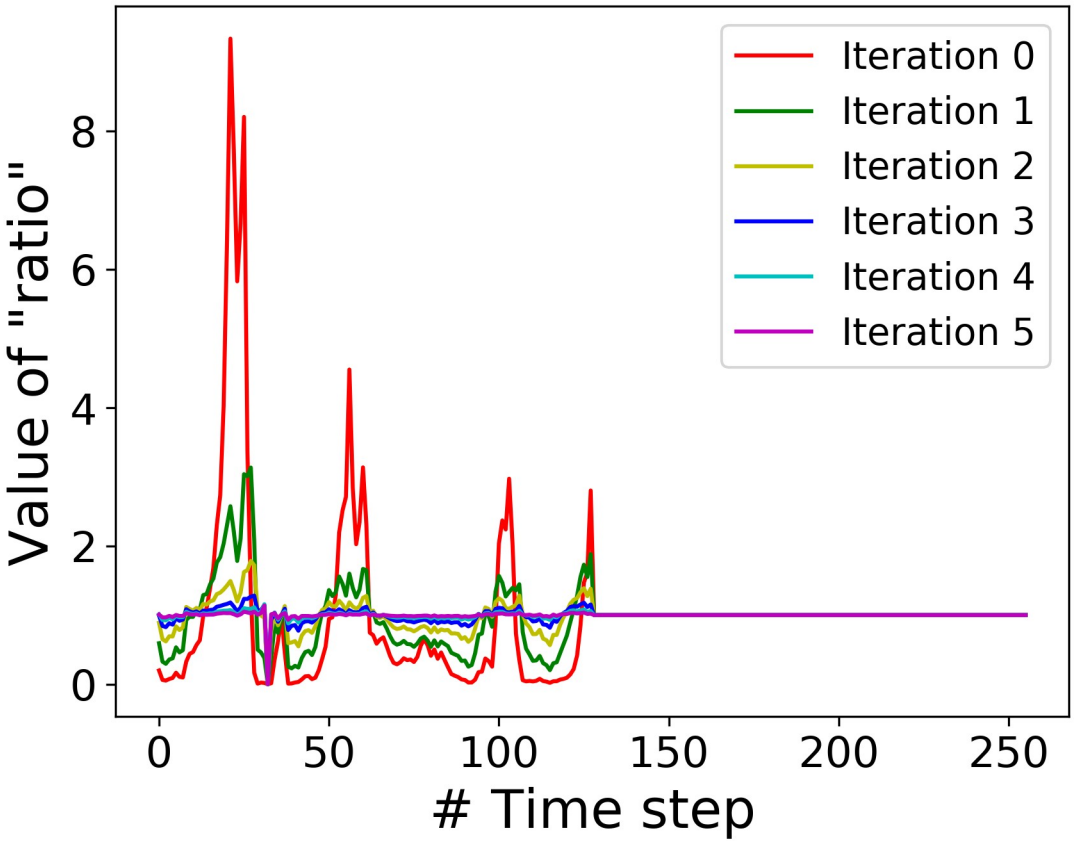

Figure 11: Illustration of the successive 'ratios' computed to obtain the simulations displayed in Fig. 10.

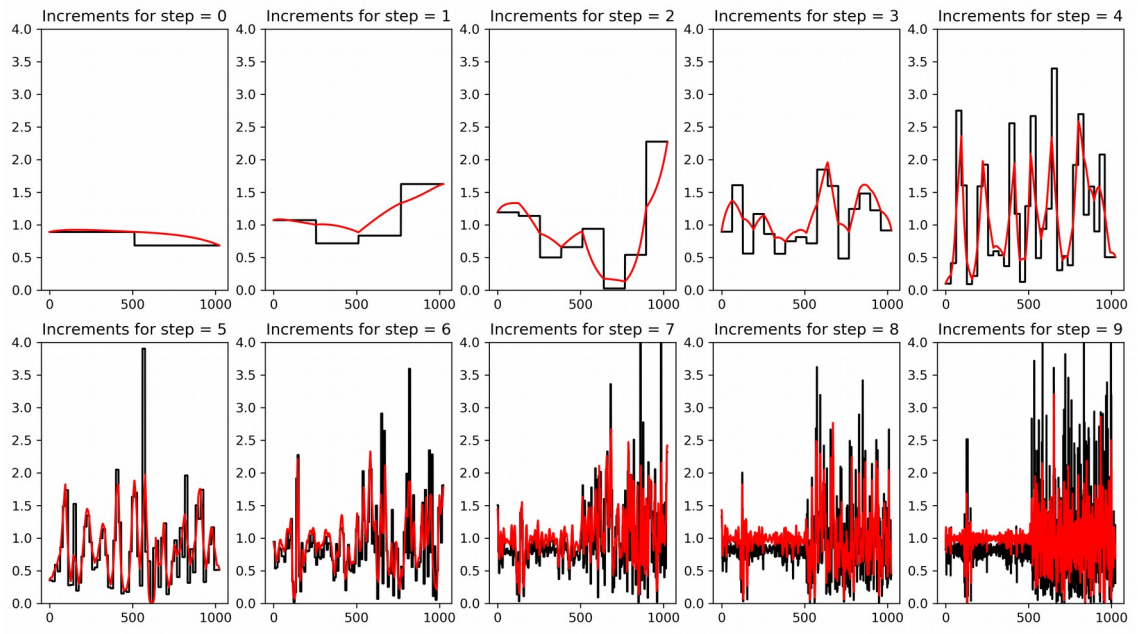

Figure 12: Increments for all the cascade steps obtained for the last iteration (i.e. the fifth) displayed in Fig. 10. Sharp increments are in black while the blunt ones are in red.

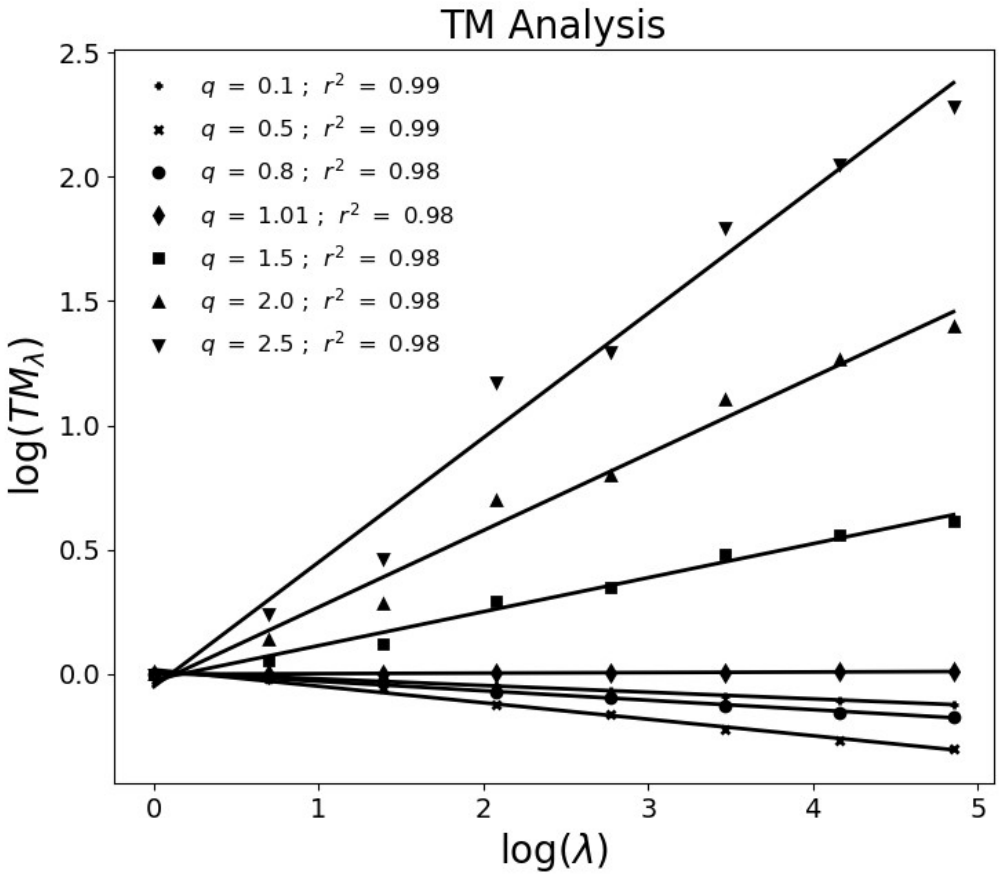

Figure 13: TM analysis, i.e. Eq. 2 in log-log, of the first half of the data used for application in 1D.

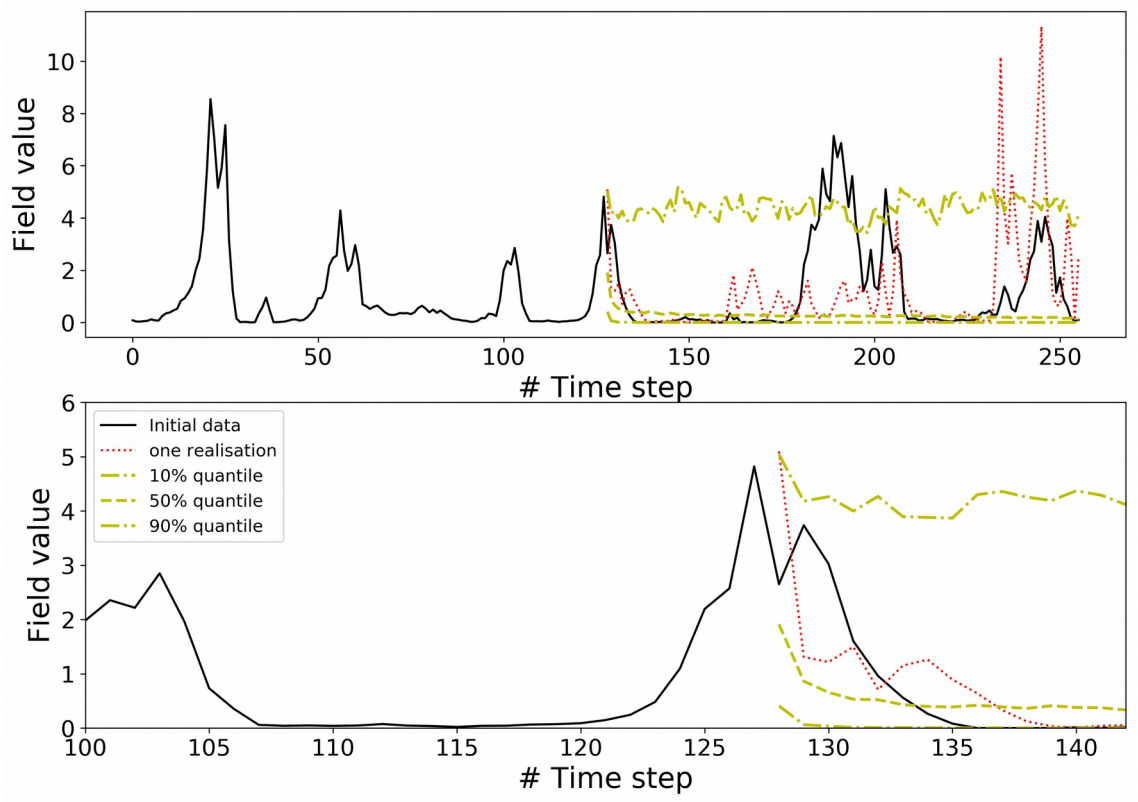

Figure 14: Illustration of the output of the newly developed algorithm on initial data (in black) corresponding to a rainfall 30 s time step series of total length 128. In red, one realisation of a realistic follow up. In yellow, 5, 50 and 95% quantiles computed over 1000 realisations. The lower part is simply a zoom of the upper one during the transition between the initial data and the stochastically generated second half.

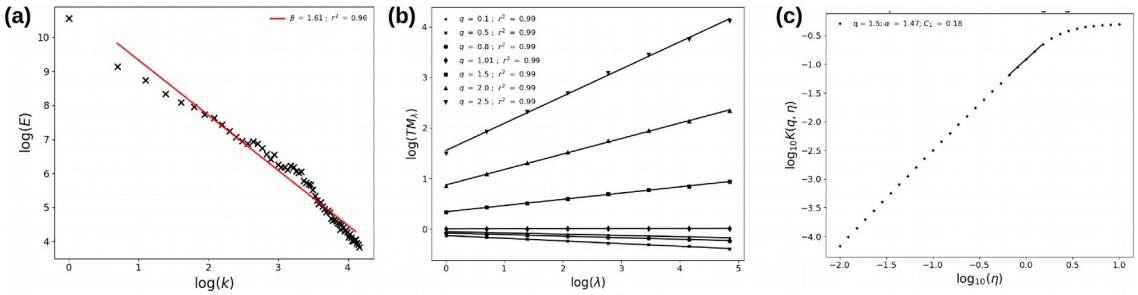

Figure 15: UM analysis of the ensemble of 1000 simulated guessed portion of the field in 1D (one sample is visible in red in Fig. 14. (a) Spectral analysis, i.e. Eq. 11 in log-log. (b) TM analysis, i.e. Eq. 2 in log-log and (c) DTM curve, i.e. Eq. 5 in log-log.

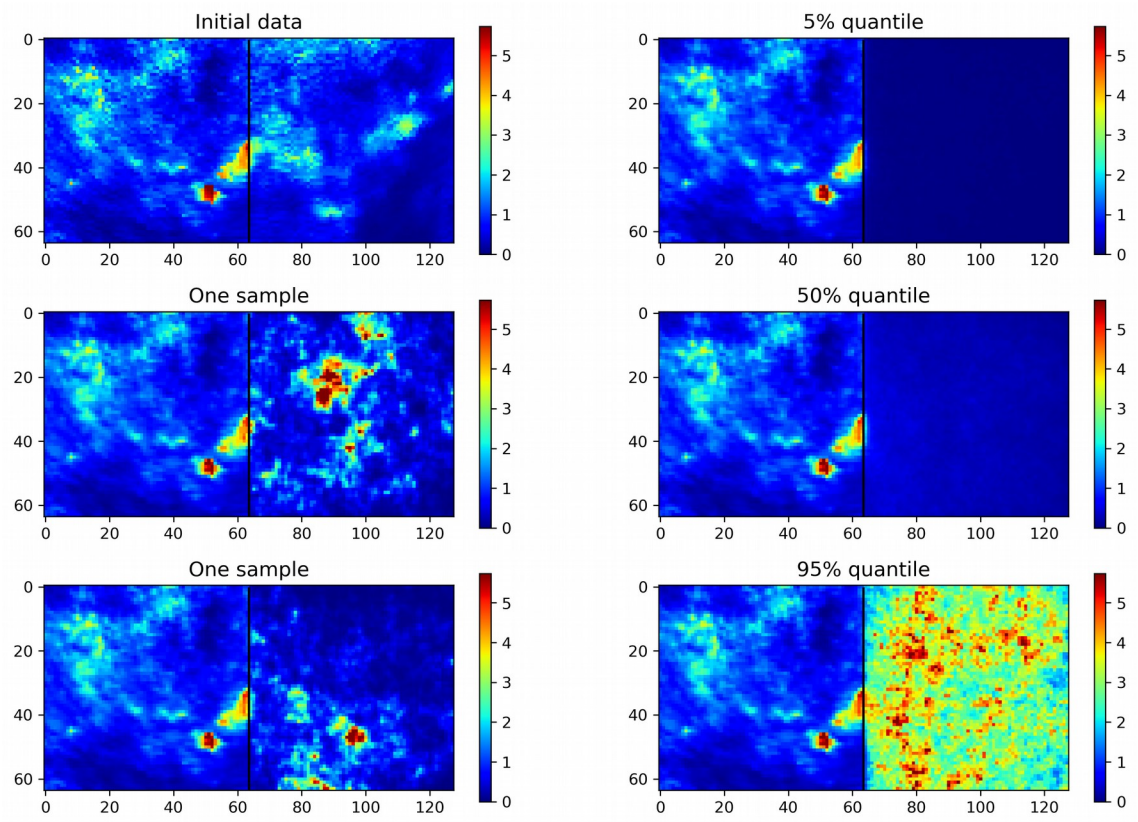

Figure 16: Illustration of the outputs of the newly developed algorithm on initial data (top left) corresponding to a radar rainfall map of 64 x 64 pixels. Only the left half (black vertical line corresponds to the split) is used, and the right half is here only for comparison purpose. Two specific realisations, as well as the 5, 50 and 95 % quantiles computed over 100 realisations are displayed.

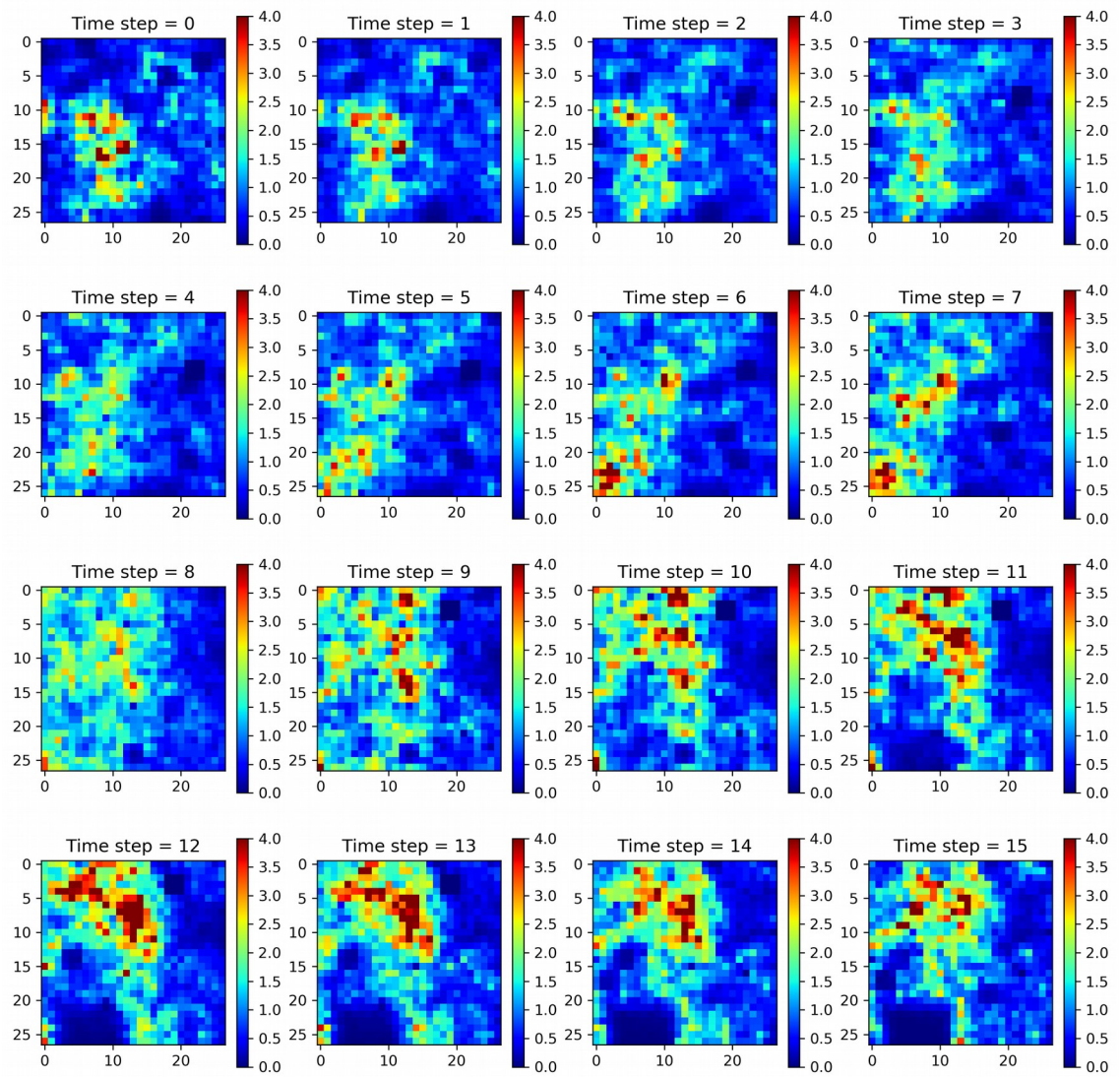

Figure 17: Illustration of the implementation of the newly developed algorithm in a space-time framework. Numerical simulations of a field made of 27 x 27 pixels over 8 time steps (from 1 to 7 in) are used as input for the algorithm to generate the next 8 (from 8 to 15).$\alpha = 1.7$, $C_1 = 0.9$ (meaning that the actual C_1 of the final field is 0.083, see Eq. 18), and $h = 4$ are used as parameters.